

Projectile Performance, Stability, and Free-Flight Motion Prediction Using Computational Fluid Dynamics

Paul Weinacht*

U.S. Army Research Laboratory, Aberdeen Proving Ground, Maryland 21005

With the recent development of capabilities for predicting damping derivatives, it is now possible to predict the stability characteristics and free-flight motion for projectiles using data that are derived solely from computational fluid dynamics (CFD). As a demonstration of the capability, results are presented for a family of axisymmetric projectiles in supersonic flight. The particular configuration selected has been extensively tested in aeroballistic ranges, and high-quality experimental data have been obtained. Thin-layer Navier–Stokes techniques have been applied to compute the attached viscous flow over the forebody of the projectile and the separated flow in the projectile base region. Parameters that characterize the in-flight motion are subsequently evaluated using the predicted aerodynamic coefficients, including the gyroscopic and dynamic stability factors and the projectile's fast- and slow-mode frequencies and damping coefficients. These parameters are then used to predict the free-flight motion of the projectile. In each case, the computational approach is validated by comparison with experimental data, and very good agreement between computation and experiment is found. It is believed that this demonstration represents the first known instance of a viscous CFD approach being applied to predict all of the necessary data for performance of linear aerodynamics stability and trajectory analyses.

Nomenclature

a_∞	=	freestream speed of sound
C_D	=	drag coefficient
C_{D0}	=	zero-yaw drag coefficient
C_l	=	net roll moment coefficient
C_{l_p}	=	roll damping moment coefficient
C_{m_α}	=	slope of the pitching moment coefficient with angle of attack
$C_{m_q} + C_{m_{\dot{\alpha}}}$	=	pitch-damping moment coefficient sum
\tilde{C}_m	=	pitching moment coefficient
C_{N_α}	=	slope of the normal force coefficient
$C_{N_q} + C_{N_{\dot{\alpha}}}$	=	pitch-damping force coefficient sum
$C_{n_{pa}}$	=	Magnus moment coefficient
\tilde{C}_n	=	side moment coefficient
$C_{Y_{pa}}$	=	Magnus force coefficient
D	=	projectile diameter
$\hat{E}, \hat{F}, \hat{G}$	=	flux vectors in transformed coordinates
e	=	total energy per unit volume
\hat{H}	=	source term in Navier–Stokes (N–S) equations
K_{10}, K_{20}	=	amplitude of fast- and slow-yaw arms
L	=	body length
M	=	freestream Mach number
p	=	spin rate, as used in roll equations
q	=	vector of dependent variables
Re	=	Reynolds number, $a_\infty \rho_\infty D / \mu_\infty$
\hat{S}	=	viscous flux vector
s	=	distance down range
s_d	=	dynamic stability factor
s_g	=	gyroscopic stability factor
u, v, w	=	velocity components in x, y, z directions
V	=	freestream velocity
x, y, z	=	axial, horizontal, and vertical coordinates

α	=	angle of attack
β	=	yaw angle
γ	=	cosine of total angle of attack
λ_1, λ_2	=	fast and slow mode damping rates
ξ, η, ζ	=	transformed coordinates in N–S equations
ξ	=	complex angle of attack
ρ	=	density
ϕ_{10}, ϕ_{20}	=	phase angle of fast- and slow-mode arms
ϕ'_1, ϕ'_2	=	fast- and slow-mode frequencies

Superscripts

\cdot	=	rate of change with respect to time
$'$	=	rate of change with respect to space
\sim	=	referenced to nonrolling coordinate frame

Introduction

PREDICTION of the in-flight motion of projectiles requires the determination of the aerodynamic forces and moments that act on the body during the course of its trajectory. These aerodynamic forces and moments may be determined from free-flight aerodynamics ranges,¹ wind-tunnel experiments,² or theoretical approaches, such as computational fluid dynamics (CFD). In the supersonic-flight regime, static aerodynamic coefficients such as drag and pitching moment have been routinely computed using CFD for a number of years.^{3,4} Much less routine are predictions of dynamic aerodynamic coefficients, such as the pitch damping and Magnus coefficients. A computational capability for predicting the Magnus forces and moments for smooth medium- and large-caliber flight bodies has existed since the early 1980s.^{3,4} With the recent development of capabilities for predicting damping derivatives,⁵ it is now possible to predict the stability characteristics and free-flight motion for projectiles using data that are derived solely from CFD.

Whereas previous research work has focused on predictions of the individual aerodynamic coefficients, the focus of this paper is on the predictions of aerodynamic performance, in particular, aerodynamic stability. An attempt is made to demonstrate, through a particular case study, the suitability and accuracy of Navier–Stokes computational techniques for the prediction of projectile performance and stability. Until recently, this was not possible because methods had not been implemented to predict all of the necessary coefficients.

As a demonstration of the capability, results are presented for a family of axisymmetric projectiles in supersonic flight. The

Received 6 March 2003; revision received 29 May 2003; accepted for publication 30 May 2003. This material is declared a work of the U.S. Government and is not subject to copyright protection in the United States. Copies of this paper may be made for personal or internal use, on condition that the copier pay the \$10.00 per-copy fee to the Copyright Clearance Center, Inc., 222 Rosewood Drive, Danvers, MA 01923; include the code 0022-4650/04 \$10.00 in correspondence with the CCC.

*Aerospace Engineer, Aerodynamics Branch, Ballistics and Weapons Concepts Division, Weapons and Materials Research Directorate. Associate Fellow AIAA.

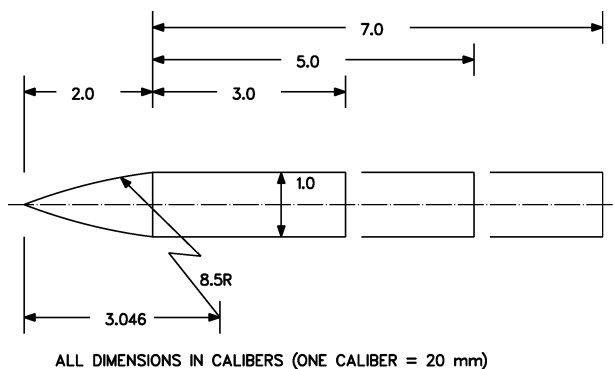


Fig. 1 Schematic of Army-Navy spinner rocket (ANSR) configuration.

particular configuration selected for this computational study has been extensively tested in aeroballistic ranges and high-quality experimental data have been obtained.¹ The configuration consists of 5-, 7- and 9-caliber length versions. Three different centers of gravity were tested for each body length by varying the mass distribution. A schematic of the configuration is shown in Fig. 1.

The computational results were obtained by applying a parabolized Navier-Stokes (PNS) approach to compute the attached viscous flow over the forebody of the projectile. Aerodynamic forces and moments were then extracted from the computed flowfields by integration of the predicted pressure and shear stresses acting on the projectile surface. To compute the recirculating flow at the base of the projectile and subsequently the base drag, a time-marching Navier-Stokes approach was applied.

Parameters that characterize the in-flight motion are subsequently evaluated using the predicted aerodynamic coefficients, including the gyroscopic and dynamic stability factors and the projectile's fast- and slow-mode frequencies and damping coefficients. These parameters are then used to predict the free-flight motion of the projectile. In each case, the computational approach is validated by comparison with experimental data.

Computational Approach

The supersonic viscous flowfield about the projectile configuration was obtained by applying a PNS technique to determine the attached flowfield over the projectile forebody and a time-marching Navier-Stokes technique to determine the recirculating flow in the base region. Both of these numerical techniques are briefly described.

PNS Approach

Computation of the attached viscous flowfield about the projectile forebody was accomplished by solving the thin-layer Navier-Stokes equations using the PNS technique of Schiff and Steger.⁶ With use of the PNS technique, computational results are obtained by marching through the grid from the projectile nose to the base. This technique is applicable in the supersonic flow regime and requires that the flowfield contain no regions of flow separation in the axial direction. Because the computational approach requires only a single sweep through the computational grid, it is very efficient, compared with time-marching approaches that require many sweeps through the grid.

As is standard practice, prediction of the static aerodynamic coefficients, such as pitching moment and normal force coefficients, are performed by computing the flowfield about the projectile at a constant angle of attack. The Magnus coefficients are obtained from a computation of the flowfield at a constant angle of attack and spin rate. Because the static aerodynamics for spinning axisymmetric bodies are generally invariant with spin rate, it is possible to obtain the static aerodynamic coefficients and the Magnus coefficients from a single computation. The pitch-damping coefficients are determined from the side force and moment acting on the projectile undergoing steady coning motion. Steady coning motion is defined as the motion performed by a missile flying at a constant angle with

respect to the freestream velocity vector and undergoing a rotation at a constant angular velocity about a line parallel to the freestream velocity vector and coincident with the projectile's c.g. Coning motion is, in fact, a specific combination of two orthogonal planar pitching motions plus a spinning motion. From linear flight mechanics theory, it can be shown that the pitch-damping coefficients are related to the side force and moment due to steady coning motion.⁵

The flowfield predictions of the projectile in steady coning motion have been performed in a novel rotating coordinate frame that rotates at the roll rate or coning rate of the projectile. The fluid flow relative to the rotating coordinate frame does not vary with time, allowing the steady (non-time-varying) Navier-Stokes equations to be applied. To implement the rotating coordinate frame, the governing equations have been modified to include the effect of centrifugal and Coriolis forces. The steady, thin-layer Navier-Stokes equations are

$$\frac{\partial \hat{E}}{\partial \xi} + \frac{\partial \hat{F}}{\partial \eta} + \frac{\partial \hat{G}}{\partial \zeta} + \hat{H} = \frac{1}{Re} \frac{\partial \hat{S}}{\partial \zeta} \quad (1)$$

Here \hat{E} , \hat{F} , and \hat{G} are the inviscid flux vectors and \hat{H} is the source term containing the Coriolis and centrifugal force terms, which result from the rotating coordinate frame. Each of these matrices is a function of the dependent variables represented by the vector $q(\rho, \rho u, \rho v, \rho w, e)$. Further details of the flux terms and the source term containing the centrifugal and Coriolis forces are given in Refs. 6 and 5, respectively.

The thin-layer equations are solved using the PNS technique of Schiff and Steger.⁶ Following the approach of Schiff and Steger, the governing equations, which have been modified here to include the Coriolis and centrifugal force terms, are solved using a conservative, approximately factored, implicit finite difference numerical algorithm as formulated by Beam and Warming.⁷ A fully turbulent boundary layer has been modeled using the Baldwin-Lomax turbulence model.⁸

The computations presented here were performed using a shock-fitting procedure reported by Rai and Chaussee.⁹ This procedure solves the five Rankine-Hugoniot jump conditions, two geometric shock-propagation conditions, and one compatibility equation to determine the values of the five dependent variables immediately behind the shock, as well as the position of the shock. The shock-fitting procedure was appropriately modified when coning motion was employed.⁵

The computational results presented here were obtained using a grid that consisted of 60 points between the body and the shock. In the circumferential direction, gridding was performed over the entire body (360 deg) using 36 points spaced at 10-deg increments. Approximately 75 axial marching steps were used for each caliber of body length. Because several of the aerodynamic coefficients are strongly influenced by viscous effects, the boundary layer was adapted by monitoring the nondimensional boundary-layer coordinate y^+ along the leeside of the body and adjusting the normal grid spacing so that the y^+ was about 3. This approach has been successfully applied in previous studies.³ The computations have been performed on a variety of computer platforms. Typical solutions for a single set of conditions (Mach number, coning rate, angle of attack, etc.) required 5–10 min total CPU time on a Cray SV1 computer.

The selection of grid parameters for the current study is consistent with those used in the previous studies that focused on the individual aerodynamics coefficients.^{3–5} The grid requirements shown in these previous studies indicate that accurate results for the complete set of aerodynamics coefficient can be obtained with a single grid. As part of the current effort, a grid refinement study for the $L/D = 9$ body, middle c.g. position was also performed. A more refined grid, with 90 points between the body and the shock, 72 circumferential points and 150 axial marching steps for each caliber of body length, was utilized. A comparison of the results obtained with the baseline and refined grids indicated a maximum difference of less than 1.5% between the two complete sets of aerodynamic coefficients.

Time-Marching Approach

For the recirculating flow in the base region of the flowfield, the PNS technique can no longer be used, and a more generally

applicable approach such as the time-marching technique must be applied. The time-marching technique is based on the unsteady or time-dependent Navier–Stokes equations. For steady flow applications, such as those discussed here, the solution is obtained by marching an initial “guessed” solution to a final converged solution in a time-iterative manner. This requires the entire flowfield to be updated at each time step, and numerous time steps are required as the solution evolves to the converged steady-state result. Because of this, the time-marching approach is much more computationally intensive in terms of its run times and computer memory requirements than the PNS technique.

For the predictions presented here, the time-dependent approach was applied to compute the axisymmetric (zero-angle-of-attack) base flow as a means of evaluating the zero-yaw drag. The small, but measureable, effect of yaw on drag was not considered in this study. The effect of the base flow on the other coefficients was also assumed to be small.

The particular time-marching technique applied here is the implicit, partially flux-split, upwind numerical scheme developed by Ying et al.¹⁰ and Sahu and Steger.¹¹ The technique is based on the flux-splitting approach of Steger and Warming¹² and is often referred to as the F3D technique. The upwind scheme provides natural numerical dissipation, better stability properties, and better computational efficiency compared with implicit central-differencing schemes.^{10–12}

The technique is based on the time-dependent thin-layer Navier–Stokes equations

$$\frac{\partial \hat{q}}{\partial t} + \frac{\partial \hat{E}}{\partial \xi} + \frac{\partial \hat{F}}{\partial \eta} + \frac{\partial \hat{G}}{\partial \zeta} + \hat{H} = \frac{1}{Re} \frac{\partial \hat{S}}{\partial \zeta} \quad (2)$$

The flux-splitting algorithm of the F3D approach reduces the computational requirements by eliminating one of the three implicit inversions associated with the central difference Beam–Warming algorithm.⁷ The two-factor implicit algorithm involves two sweeps through the grid at each time step. The first sweep involves inverting the block tridiagonal system of equations in the ζ direction along grid lines of constant ξ and η to determine the intermediate solution variable. During the second sweep, a second block tridiagonal system of equations is inverted in the η direction along grid lines of constant ξ and ζ and to determine the dependent variable.

The particular version of the code applied here has a multizone capability that allows the computational grid to be decomposed into smaller blocks. This allows greater flexibility in gridding of flight bodies, particularly when it is desirable to preserve sharp corners. The multizone capability also allows the computer memory requirement for the computation to be reduced because only one zone needs to be in memory at a time and the other zones can be stored on disk. This capability was implemented by Sahu and Steger.¹¹

The zonal gridding approach was used to compute the recirculating viscous flow in the base region. A large grid zone was located in the base region and extended axially from the projectile base 6.35 calibers downstream. In the radial direction, the grid extended outward from the axis of symmetry to a radial location 3.5 calibers above the base corner. To allow the flow to expand properly around the base corner, a small zone, one body diameter in length, was placed on the forebody upstream from the base corner. This grid had a one-plane overlap with the base grid and a one-to-one mapping of the grid points in the overlap region. The dimensions of the base grid were 120 axial points, 50 radial points along the base, and 50 radial points above the base corner. The forebody grid had 30 axial points and 50 radial points. Clustering of the grid points in the radial direction was performed to resolve the boundary layer on the forebody and the shear layer in the base region. The algebraic turbulence model of Chow¹³ was applied in the base region.

Results

As a first step in evaluating the aerodynamic performance of a flight vehicle, the aerodynamic force and moment coefficients must be evaluated. The aerodynamic coefficients allow forces and moments due to complicated three-dimensional motions to be charac-

terized as a combination of aerodynamic forces and moments due to simple specific motions. The individual aerodynamic coefficients can provide insight into the aerodynamic performance of the flight vehicles.

Aerodynamic Moments

For symmetric missiles, the aerodynamic moments are typically modeled using the following moment expansion, which is cast in a nonrolling coordinate frame.¹⁴ The moment formulation employs complex variables to separate the transverse moment components \tilde{C}_m and \tilde{C}_n , which produce rotations in the vertical and horizontal planes, respectively. The moment about the longitudinal axis of the vehicle, C_l , can be treated separately. Thus,

$$\tilde{C}_m + i\tilde{C}_n = [(pD/V)C_{n_{pa}} - iC_{m_{\alpha}}]\tilde{\xi} - (i/\gamma)[C_{m_q} + \gamma C_{m_{\dot{\alpha}}}]\tilde{\xi}' \quad (3)$$

$$C_l = (pD/V)C_{l_p} \quad (4)$$

In the moment formulation, the pitching moment coefficient $C_{m_{\alpha}}$ produces a moment proportional to the complex angle of attack $\tilde{\xi}$. For small-angle-of-attack flight, the cosine of the total angle of attack γ is nearly one. This allows the pitch–damping moment coefficient, $C_{m_q} + C_{m_{\dot{\alpha}}}$, which produces moments proportional to the angular rate $\tilde{\xi}'$, to be treated as a single coefficient. The Magnus moment coefficient $C_{n_{pa}}$ accounts for a side moment due to flow asymmetries from a combination of spin and angle of attack.

Over the past decade and a half, CFD techniques have been developed to predict the various aerodynamic coefficients just discussed. The pitching moment coefficient $C_{m_{\alpha}}$ has been routinely determined for various configurations and flight regimes for well over a decade. The prediction of the Magnus coefficients for axisymmetric projectiles at supersonic velocities was demonstrated in the early 1980s.³ This development was motivated primarily by the failure of theoretical methods to properly predict the Magnus coefficients for boattailed projectiles,³ although reasonable predictions using theoretical methods are possible for cylindrical afterbodies in some flight regimes.^{15,16} The Magnus problem is still a research topic for complicated vehicles and at transonic velocities.

More recently, techniques for predicting the pitch–damping coefficient, $C_{m_q} + C_{m_{\dot{\alpha}}}$, based on the solution of the Navier–Stokes equations have been developed.⁵ Although the development of a capability to predict each individual aerodynamic coefficient can be considered an important research accomplishment, it was not possible to predict the stability characteristics of projectiles using CFD until a complete capability for predicting all of the aerodynamic coefficients was developed. The prediction of the pitch–damping coefficient represented that final step. Theoretical methods such as slender body theory can also be applied to predict the pitch–damping coefficients, although only qualitative comparisons can be made with experimental and computational results.¹⁷ Semi-empirical methods^{18,19} offer an alternative approach for aerodynamic coefficient prediction, and these methods continue to evolve. Note that the availability of the recent CFD predictions of pitch–damping has aided in the improvement of these semi-empirical methods.¹⁹

Figures 2–4 show results of CFD predictions for pitching moment, Magnus moment, and pitch–damping moment coefficients performed as part of the current study. Results for a free-flight Mach number of 1.8 are shown for each of the three c.g. and body lengths. In general, the CFD predictions appear to be in good agreement with the experimental data obtained from range firings¹ of these projectiles. Results obtained at Mach 2.5 also show similar agreement with the range data.

The aerodynamic moment about the longitudinal axis of an axisymmetric vehicle can be modeled using a single aerodynamic coefficient. The roll–damping coefficient C_{l_p} represents the aerodynamic moment that opposes the spinning motion of the vehicle. For axisymmetric flight bodies, the roll–damping coefficient is produced purely by the viscous stresses acting circumferentially on the body surface. From a modeling standpoint, proper prediction

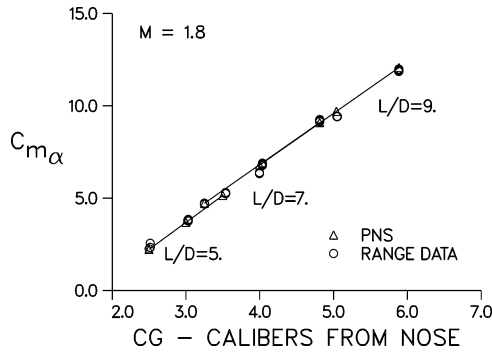


Fig. 2 Pitching moment coefficient vs c.g. position, $M = 1.8$, ANSR.

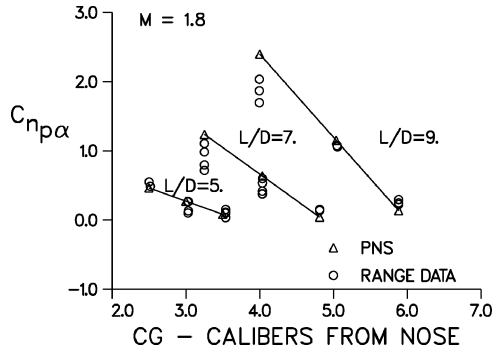


Fig. 3 Magnus moment coefficient vs c.g. position, $M = 1.8$, ANSR.

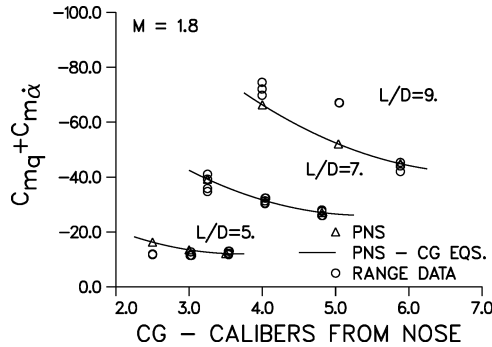


Fig. 4 Pitch-damping moment coefficient vs c.g. position, $M = 1.8$, ANSR.

of the roll-damping coefficient requires adequate grid resolution of the boundary layer. A comparison of the predicted roll-damping coefficient with range data is shown in Fig. 5. Both the computational predictions and the range data show a nearly linear increase in the roll-damping coefficient with increasing body length. The predicted result shows an overprediction of about 10%. Similar results were observed at Mach 2.5. The predictions showed less than a 1% variation in the roll-damping coefficient at angles of attack to 6 deg.

Aerodynamic Forces

The aerodynamic forces can also be described in a manner that is analogous to the aerodynamic moments. The transverse force components C_Y and C_Z act along the \hat{y} and \hat{z} axes of the non-rolling coordinate frame and consist of components proportional to the complex yaw ξ and yawing rate ξ' . The third force component, which acts along the axial direction, is loosely coupled to the transverse forces and can be treated separately. This force component consists predominantly of the drag force. Thus,

$$\tilde{C}_Y + i\tilde{C}_Z = -[C_{N_\alpha} + i(pD/V)C_{Y_{p\alpha}}]\tilde{\xi} - (1/\gamma)[C_{N_q} + \gamma C_{N_{\dot{\alpha}}}]\tilde{\xi}' \quad (5)$$

$$C_X = -C_D \quad (6)$$

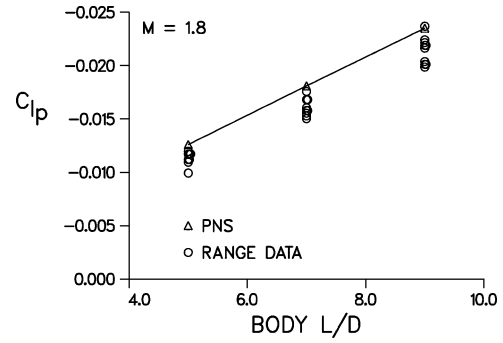


Fig. 5 Roll-damping moment coefficient vs body length, $M = 1.8$, ANSR.

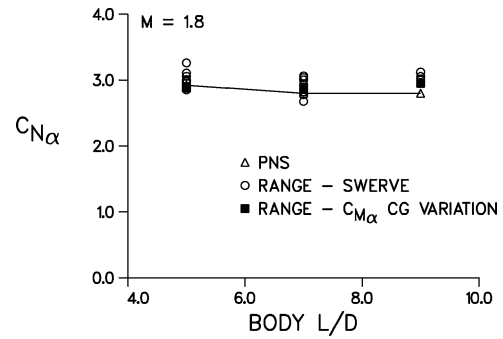


Fig. 6 Normal force coefficient vs body length, $M = 1.8$, ANSR.

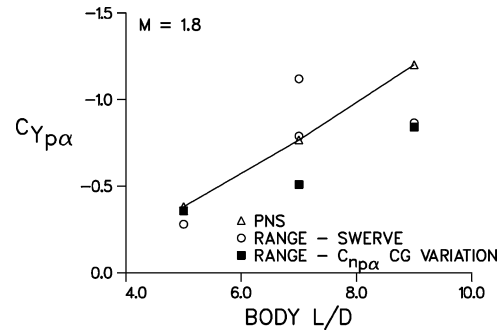


Fig. 7 Magnus force coefficient vs body length, $M = 1.8$, ANSR.

The normal force coefficient C_{N_α} acts normal to the longitudinal axis of the body in the pitch plane. The force expansion also contains a damping force coefficient, $C_{N_{\dot{\alpha}}} + C_{N_q}$, that produces a force proportional to the yawing rate ξ' . The Magnus force coefficient $C_{Y_{p\alpha}}$ accounts for the side force produced by a combination of spin and yaw.

Figures 6 and 7 show comparisons of the predicted and experimentally determined normal force and Magnus force coefficients at Mach 1.8 as a function of body length. The predicted normal force coefficient is predicted to be within the scatter of the range data and shows little influence of body length. Both the predicted and experimentally determined Magnus force coefficient increase with body length. The Magnus force determined from the variation of the Magnus moment with c.g. location is about 30% less than the predictions for the $L/D = 7$ and $L/D = 9$ bodies. The Magnus force coefficients determined from the swerving (c.g.) motion for individual shots shows significant scatter, indicating the difficulty in accurately determining this coefficient. The pitch-damping force coefficient is not shown because it does not influence the projectile motion in a measurable manner. Comparisons of predictions with experimental data are presented in Ref. 5.

The drag coefficient is also very important for predicting projectile flight performance because it is one of the primary aerodynamic coefficients affecting range. The drag coefficient is also required

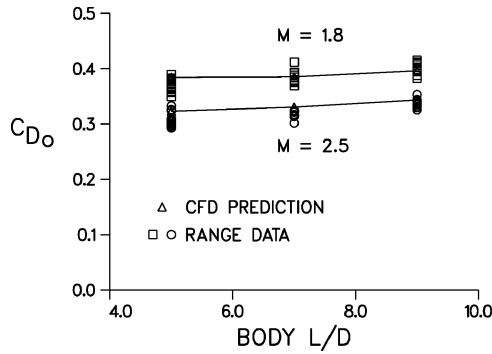


Fig. 8 Zero-yaw drag coefficient vs c.g. position, $M = 1.8$ and $M = 2.5$, ANSR.

for the stability assessment, although its effect is small. The total drag on the projectile is composed of contributions from the forebody and the base. The forebody drag consists of both pressure and viscous drag components. The base drag results from the pressure acting on the projectile base. The forebody drag can be predicted using the PNS technique. The recirculating flow in the base region is predicted using the time-marching technique from which the base drag can be determined.

A comparison of the predicted zero-yaw drag with range results is shown in Fig. 8. Drag predictions at Mach 1.8 and 2.5 are shown as a function of body length. Both the experimental results and the computational results show a slight increase in zero-yaw drag with increasing body length and decreasing Mach number. The computed drag coefficient is predicted to within the accuracy of the range data. The increase in the drag with body length is due primarily to the increase in the wetted surface of the longer body. The predicted results showed only minor variations in the base drag with body length.

At Mach 1.8 for the $L/D = 9$ body, the pressure and viscous forebody drag account for 39% and 25% of the total drag with the base drag accounting for the remaining 36% of the drag. Predictions of the forebody pressure drag are within 1% of previous predictions using empirical²⁰ or inviscid¹ approaches.

An estimate of the predicted skin-friction drag C_{D_v} can be obtained using the relation developed by Charters and Kent²¹:

$$C_{D_v} = -4C_{l_p} \quad (7)$$

The estimated skin-friction drag determined from the predicted roll-damping coefficient underestimates the predicted skin-friction drag by 3–10% for the predictions presented here. (This comparison gives an indication of the accuracy of the Charters and Kent relation.) The estimated skin friction obtained from the range measurements of the roll-damping coefficient is 13–22% less than the predicted skin friction. Although these estimates indicate a potential 10% overprediction of the skin-friction drag, the contribution to the total drag would result in an overprediction of only a few percent.

Design codes²⁰ can provide a more cost-effective alternative for predicting the base drag, thus, eliminating the need for a time-dependent base drag computation. The semi-empirical approach of McCoy²⁰ appears to overpredict the base drag by 10–20% compared to the CFD result. When the estimated base drag is added to the forebody-drag CFD predictions, the total drag is overpredicted by less than 9% compared to the CFD results. For stability computations, where the drag coefficient plays a minor role, acceptable accuracy can be obtained using base drag estimates.

Stability and Free-Flight Motion

Once the aerodynamic forces and moments have been determined, the equations of motion can be integrated and the projectile's motion can be determined for various initial conditions. Because the equations of motion are nonlinear, numerical integration is usually required to predict the projectile motion from launch to impact. These nonlinearities are typically weak, and for portions of the flight

trajectory, the equations can be integrated and closed-form solutions for the projectile motion can be obtained.

For a symmetric missile, the closed-form solution for the angular response as a function of the distance down range, s , takes the following form¹⁴:

$$\begin{aligned} \tilde{\xi} &= \tilde{\xi}_g + K_1 + K_2 \approx \beta + i\alpha \\ K_1 &= K_{10} \exp[i(\phi_{10} + \phi'_1 s) + \lambda_1 s] \\ K_2 &= K_{20} \exp[i(\phi_{20} + \phi'_2 s) + \lambda_2 s] \end{aligned} \quad (8)$$

The complex variable $\tilde{\xi}$ consists of the vertical and horizontal components of the angle of attack, α and β . The angular motion contains a gravity term $\tilde{\xi}_g$, which is small and for the remainder of the discussion this term will be ignored. The second and third terms of Eq. (8) are expressions of the amplitudes of two components of the angular motion, referred to as the fast and slow modes, respectively. The complex angle of attack $\tilde{\xi}$ can be displayed graphically along with the fast- and slow-mode arms, K_1 and K_2 . Graphically, the solution is shown by Fig. 9 and is referred to as a damped epicycle. It is helpful to regard Fig. 9 as the path that the nose of the projectile would follow as it flies down range. The fast- and slow-mode frequencies of the motion, ϕ'_1 and ϕ'_2 , and the damping rates, λ_1 and λ_2 , are functions of the aerodynamic coefficients, projectile spin rate, and inertial properties of the body. Generally speaking, the frequencies are influenced by the pitching moment coefficient, whereas the damping is influenced by the Magnus and pitch-damping coefficients. The equation also contains the initial amplitudes, K_{10} and K_{20} , and phase angles, ϕ_{10} and ϕ_{20} , which result from applying the initial conditions during the integration of the equations.

Using the predicted aerodynamic coefficients, the fast- and slow-mode damping and frequencies were computed for the various body lengths, c.g., launch Mach numbers, and spin rates. Figure 10 shows the predicted slow-mode frequency plotted against the experimentally determined value. (The results are plotted in this fashion because of the large number of parameters considered here.) Points

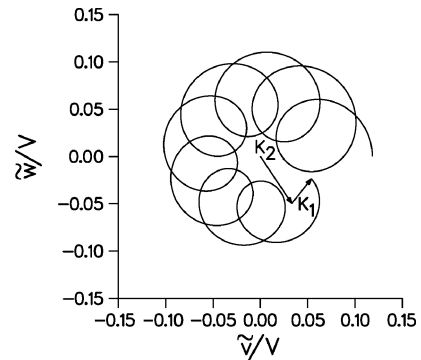


Fig. 9 Projectile angular motion epicycle.

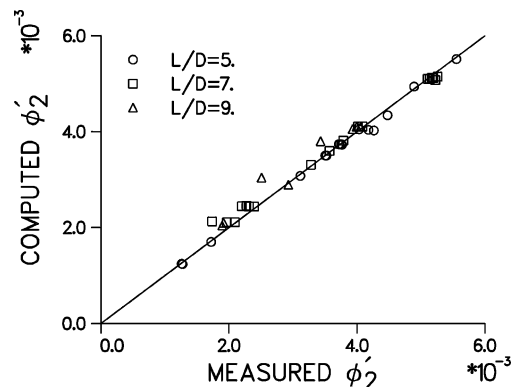


Fig. 10 Comparison of computed slow-mode frequency with measured slow-mode frequency, ANSR.

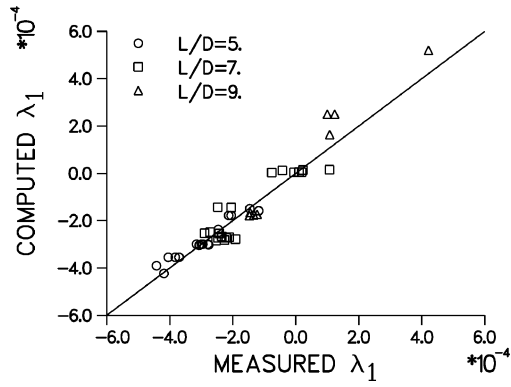


Fig. 11 Comparison of computed fast-mode damping with measured fast-mode damping, ANSR.

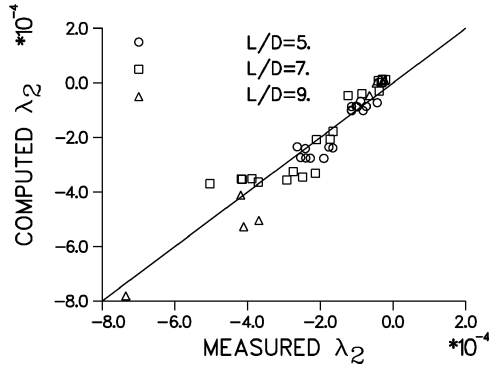


Fig. 12 Comparison of computed slow-mode damping with measured slow-mode damping, ANSR.

that fall close to the solid line indicate that the predicted value is close to the experimentally determined value.

There is good agreement between prediction and experiment. The slow-mode frequency represents the critical comparison for the frequencies because the fast-mode frequency is dominated by the spin rate, which is essentially an input parameter.

Figures 11 and 12 show comparisons of the predicted slow- and fast-mode damping of each of the bodies. The data are scattered about the solid line, indicating that the prediction is generally in good agreement with the experiment. No consistent bias between the computation and experimental data is seen. This indicates that there is no consistent underprediction or overprediction of the damping rates. Much of the scatter in the data is attributed to the uncertainty in the experimental data rather than inaccuracies in the computational approach.

Generally, from a design standpoint, predicting and controlling damping rates, rather than the frequencies, is a primary consideration. One desirable requirement is that the damping rates λ_1 and λ_2 be negative so that the angular motion does not grow during the projectile's flight. When the equations for the damping rates are algebraically manipulated, three necessary conditions can be derived, which will ensure that the damping rates are negative. Two of these conditions are

$$s_g > 1, \quad s_g = f(p, C_{m\alpha}) \quad (9)$$

$$s_g < s_d(2 - s_d), \quad s_d = f(C_{n_{pa}}, C_{m_q} + C_{m\ddot{\alpha}}) \quad (10)$$

The first condition states that the gyroscopic stability factor s_g must be greater than one for the projectile to be gyroscopically stable. The second condition also places an additional constraint on the gyroscopic stability factor through the dynamic stability factor s_d . As shown in these equations, the gyroscopic stability and dynamic stability factors are functions of the aerodynamic coefficients. Additionally, the gyroscopic stability factor is also a function of the projectile spin rate p . For typical spin-stabilized projectiles that are

statically unstable, the two stability criteria can be satisfied by adjusting the spin rate of the projectile, as long as the dynamic stability factor is between zero and two. If the dynamic stability factor is outside this bound, the projectile cannot be stabilized using spin. A third condition for stability essentially requires the pitch-damping coefficient, $C_{m_q} + C_{m\ddot{\alpha}}$, to be negative. This condition is rarely violated in practice.

The constraints on the gyroscopic stability and dynamic stability factors discussed earlier can be shown graphically on what is often termed a stability plot. Figures 13 and 14 show results as measured in the aerodynamics range and obtained from the computation. Shown are results for each of the three c.g., the three different length bodies, various spin rates, and Mach numbers of 1.8 and 2.5. For each firing, experimental and computational values of the gyroscopic stability factor s_g and the dynamic stability factor s_d were computed. It is important to realize that for a given set of conditions (body length, spin rate, launch Mach number), the computational results will yield a unique value. However, because of the scatter associated with the experimental data, each firing yields a slightly different value. Thus, the experimental results gives the appearance of having more data. It is important to realize this when comparing Figs. 13 and 14 data.

The computational and experimental results presented in Figs. 13 and 14 show that this family of projectiles is statically unstable ($s_g > 0$), but has been made gyroscopically stable by appropriate selection of the spin rate ($s_g > 1$). The results also show that all of the $L/D = 5$ projectiles are dynamically stable. (The region of dynamic stability is denoted by the shaded area in Figs. 13 and 14.) The results indicate that several of the $L/D = 7$ and $L/D = 9$ projectiles are marginally stable, although these can be stabilized by selection of a higher spin rate because the dynamic stability factor is between zero and two. Several of the $L/D = 9$ bodies are dynamically unstable and cannot be stabilized by changing the spin rate. Further examination of the data revealed that the $L/D = 9$ bodies that could not be stabilized all had the c.g. in the aftmost position. Note that the computational approach correctly predicts the stability characteristics of the various configurations for the conditions of dynamic stability, marginal dynamic stability, and dynamic instability. This demonstrates the utility of the computational approach for the purposes of stability prediction.

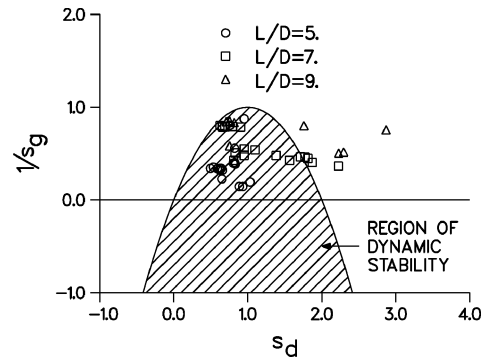


Fig. 13 Stability plot for ANSR from range data.

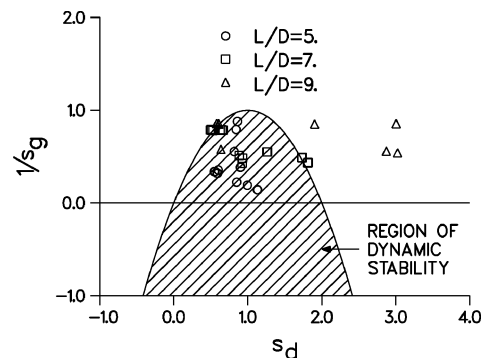


Fig. 14 Stability plot for ANSR from CFD predictions.

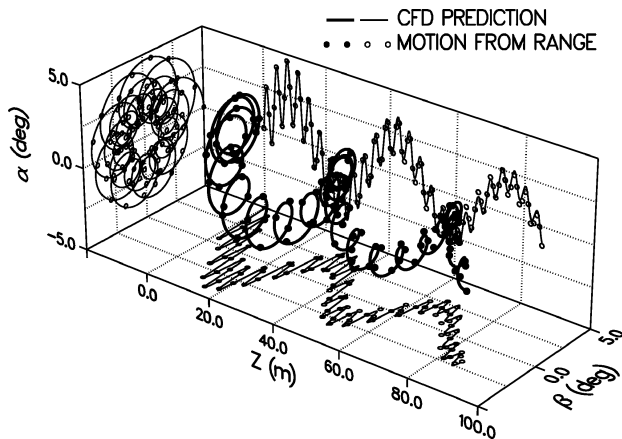


Fig. 15 In-flight angular motion, 5-caliber body, $M = 1.8$.

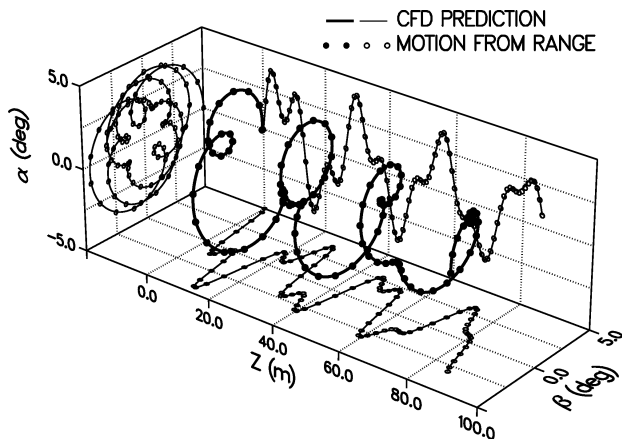


Fig. 16 In-flight angular motion, 7-caliber body, $M = 2.5$.

With the prediction of the frequencies and damping rates of the angular motion, the angular motion itself can be predicted and compared with the motion measured in the aerodynamics range. Figures 15 and 16 show the angular motion of a 5-caliber projectile launched at Mach 1.8 and a 7-caliber projectile launched at Mach 2.5. These three-dimensional plots show the vertical and horizontal components of angle of attack, α and β , as a function of the distance downrange, Z . The thickened curve displays the three-dimensional motion. Two-dimensional projections of the motion in the vertical and horizontal planes are also shown. It is useful to regard the curves shown here as the path traversed by the nose of the projectile as it flies downrange. The motion predicted using the CFD derived aerodynamic coefficients is denoted by the solid lines, whereas the motion obtained from the range firings is shown by the circular symbols. The agreement between the two motions is excellent. Comparisons of the in-flight motion at other flight conditions and for the other body geometries also showed good agreement with the experimental data.

Conclusions

CFD provides an alternate means for determining the aerodynamic performance of projectiles. This will allow projectiles to be designed with a reduced requirement for manufacturing models and performing test firings. As a test case, the aerodynamic performance of a family of axisymmetric projectiles in supersonic flight was examined. The predictions showed good agreement with range data for individual aerodynamic coefficients. Subsequently, the frequencies and damping rates of the angular motion were computed using these coefficients. The results showed good correlation with the experimental data for various body lengths, c.g. locations, Mach numbers and spin rates. The aerodynamic coefficients were also used to predict gyroscopic and dynamic stability factors. The computational approach correctly distinguished the conditions of dynamic instability, marginal dynamic stability, and dynamic stability. As a final

comparison, the in-flight angular motion for individual firings was compared with range data and showed good agreement. The results are believed to properly represent the capability for predicting the linear aerodynamics for the high-speed low-angle-of-attack flight of aerodynamically smooth axisymmetric projectiles. Additional computational effort (and, in some cases, additional research) may be required to establish the same capability at subsonic and transonic velocities or for complex geometries.

References

- ¹Murphy, C. H., and Schmidt, L. E., "The Effect of Length on the Aerodynamics Characteristics of Bodies of Revolution in Supersonic Flight," U.S. Army Ballistic Research Lab., Rept. 876, Aberdeen Proving Ground, MD, Aug. 1953.
- ²Nietubicz, C. J., and Opalka, K., "Supersonic Wind Tunnel Measurements of Static and Magnus Aerodynamic Coefficients for Projectile Shapes with Tangent and Secant Ogive Noses," U.S. Army Ballistic Research Lab., Memorandum Rept. ARBRL-MR-02991, Aberdeen Proving Ground, MD, Feb. 1980.
- ³Sturek, W. B., and Schiff, L. B., "Computations of the Magnus Effect for Slender Bodies in Supersonic Flight," *Proceedings of the AIAA Atmospheric Flight Mechanics Conference*, AIAA, New York, 1980, pp. 260–270.
- ⁴Sturek, W. B., and Mylin, D. C., "Computational Parametric Study of the Magnus Effect on Boattailed Shell at Supersonic Speeds," AIAA Paper 81-1900, Aug. 1981.
- ⁵Weinacht, P., Sturek, W. B., and Schiff, L. B., "Navier–Stokes Predictions of Pitch Damping for Axisymmetric Projectiles," *Journal of Spacecraft and Rockets*, Vol. 34, No. 6, 1997, pp. 753–761.
- ⁶Schiff, L. B., and Steger, J. L., "Numerical Simulation of Steady Supersonic Viscous Flow," *AIAA Journal*, Vol. 18, No. 12, 1980, pp. 1421–1430.
- ⁷Beam, R., and Warming, R. F., "An Implicit Factored Scheme for the Compressible Navier–Stokes Equations," *AIAA Journal*, Vol. 16, No. 4, 1978, pp. 85–129.
- ⁸Baldwin, B. S., and Lomax, H., "Thin Layer Approximation and Algebraic Model for Separated Turbulent Flows," AIAA Paper 78-257, Jan. 1978.
- ⁹Rai, M. M., and Chaussee, D. S., "New Implicit Boundary Procedure: Theory and Applications," AIAA Paper 83-0123, Jan. 1983.
- ¹⁰Ying, S. X., Steger, J. L., Schiff, L. B., and Baganoff, D., "Numerical Simulation of Unsteady, Viscous, High-Angle-of-Attack Flows Using a Partially Flux-Split Algorithm," AIAA Paper 86-2179, Aug. 1986.
- ¹¹Sahu, J., and Steger, J. L., "Numerical Simulation of Three-Dimensional Transonic Flows," *International Journal for Numerical Methods in Fluids*, Vol. 10, June 1990, pp. 855–873.
- ¹²Steger, J. L., and Warming, R. F., "Flux Vector Splitting of the Inviscid Gasdynamic Equations with Application to Finite-Difference Methods," *Journal of Computational Physics*, Vol. 40, April 1981, pp. 263–293.
- ¹³Chow, W. L., "Improvement on Numerical Computation of the Thin-Layer Navier–Stokes Equation With Special Emphasis on the Turbulent Base Pressure of a Projectile in Transonic Flight Condition," Univ. of Illinois, Contract Rept. DAAG29-81-D-0100, Urbana, IL, Nov. 1985.
- ¹⁴Murphy, C. H., "Free Flight Motion of Symmetric Missiles," U.S. Army Ballistic Research Lab., Rept. 1216, Aberdeen Proving Ground, MD, July 1963.
- ¹⁵Vaughn, H. R., and Reis, G. E., "A Magnus Theory," AIAA Paper 73-124, Jan. 1973.
- ¹⁶Sturek, W. B., Dwyer, H. A., Kayser, L. D., Nietubicz, C. J., Reklis, R. P., and Opalka, K. O., "Computations of Magnus Effect for a Yawed, Spinning Body of Revolution," *AIAA Journal*, Vol. 16, No. 7, 1978, pp. 687–692.
- ¹⁷Weinacht, P., "Navier–Stokes Predictions of the Individual Components of the Pitch-Damping Sum," *Journal of Spacecraft and Rockets*, Vol. 35, No. 5, 1998, pp. 598–605.
- ¹⁸Whyte, R. H., "‘Spinner’—A Computer Program for Predicting the Aerodynamic Coefficients of Spin Stabilized Projectiles," General Electric Co., Class 2 Rept. 69APB3, Burlington, VT, Aug. 1969.
- ¹⁹Moore, F. G., and Hymer, T. C., "The 2002 Version of the Aeroprediction Code: Part I—Summary of New Theoretical Methodology," U.S. Naval Surface Warfare Center, Rept. NSWCDD/TR-01/108, Dahlgren, VA, March 2002.
- ²⁰McCoy, R. L., "‘MC DRAG’—A Computer Program for Estimating the Drag Coefficients of Projectiles," U.S. Army Ballistic Research Lab., Technical Rept. ARBRL-TR-02293, Aberdeen Proving Ground, MD, Feb. 1981.
- ²¹Charters, A. C., and Kent, R. H., "The Relation Between the Skin Friction and the Spin Reducing Torque," U.S. Army Ballistic Research Lab., Rept. 287, Aberdeen Proving Ground, MD, July 1942.